

Vision-Based Surgical Suture Looping Through Trajectory Planning for Wound Suturing

Bo Lu, Henry K. Chu[✉], Member, IEEE, K. C. Huang, and Li Cheng

Abstract—Robot-assisted surgery has revolutionized the field of surgery over the past few decades. Despite many successes, achieving full automation in these surgeries remains a challenging task. In this paper, a dynamic approach is proposed to automate knot tying with an in-house robot vision system. Through efficient path planning and coordination between two grippers, the workspace required for constructing the suture loop can be reduced while issues such as suture slippage and collisions between instruments can be eliminated. Visual images were employed to monitor the two grippers in real time and their positions were evaluated using transformation matrices obtained experimentally. A linear quadratic control scheme was applied to optimize the tracking performance of the two grippers. From the experiments, this visual evaluation method can achieve a position accuracy of 1 mm in the workspace. The proposed algorithm was evaluated and automatic suture looping operation was successfully performed in all six trials. Different parameters in the control scheme were also examined by introducing external impulse disturbances during the knot-tying process. This proposed knot-tying approach demonstrates a simple and efficient way to construct a suture knot in a minimal workspace.

Note to Practitioners—A surgical operation usually takes several hours to complete, which is a test of surgeon's endurance. To better assist surgeons, several repetitive surgical tasks can be performed automatically with a robotic system. This paper presents a new method for robot-assisted surgical knot tying in a confined environment. Through simultaneous manipulation and trajectory planning of the two surgical grippers, suture loops were constructed while keeping the suture in tension. Images were employed to guide the grippers in completing the knot-tying process with high precision. Experiments were conducted to demonstrate the automated suture looping operation with the system and the proposed method. The robustness of the method was also examined by introducing impulse disturbances and occlusions during the experiments. This proposed method does not require complicated hardware setup, allowing easy implementations on various surgical systems.

Index Terms—Automatic control, collision avoidance, path planning, robot vision systems, suture looping.

Manuscript received April 16, 2018; accepted May 15, 2018. Date of publication June 15, 2018; date of current version April 5, 2019. This paper was recommended for publication by Associate Editor H. Ren and Editor S. Yu upon evaluation of the reviewers' comments. This work was supported by the Research Grant Council of the Hong Kong Special Administrative Region, China under Grant 25204016. (*Corresponding author: Henry K. Chu*)

The authors are with the Department of Mechanical Engineering, The Hong Kong Polytechnic University, Hong Kong (e-mail: henry.chu@polyu.edu.hk).

Color versions of one or more of the figures in this paper are available online at <http://ieeexplore.ieee.org>.

Digital Object Identifier 10.1109/TASE.2018.2840532

I. INTRODUCTION

INNOVATIONS in medical technology are the significant drives to the rapid development of advanced robotic tools and systems for clinical applications. In particular, robot-assisted surgery (RAS) is increasingly adopted by surgeons to overcome the limitations of manual surgery [1]. Minimal invasive surgeries such as laparotomy, cardiology, and urology are seeking assistances from robots with the aim of offering higher precision, dexterity, and flexibility. The first robot introduced for surgical use was the Automated Endoscopic System for Optical Positioning. This clinical equipment serves as a camera holder in an endoscopic environment, which can be automated for optimal positioning [2]. Afterward, different commercial and in-house surgical robots were developed [3]. Nowadays, surgical robots with visual guidance and sensory feedback have become the standard in RAS. For instance, Mayer *et al.* [4] proposed to use KUKA robot and PHANTOM device as the platform to simulate the robotic heart surgery. Force sensors were added to monitor the force during the operation. Hynes *et al.* [5] developed a system that was capable of performing surgical tasks under minimal human supervision. The system employed both visual and kinematic models to coordinate the robot motion for tying a surgical knot. While these proposed robots were able to perform selected surgical tasks, achieving automations can help to enhance the accuracy and the efficiency by reducing human errors.

The commercial da Vinci surgical system was first introduced in 2000 for clinical practice [6], [7]. The dexterity of the system enables surgeons to perform more challenging endoscopic surgeries such as prostatectomy manipulations [8], [9], thoracic operations [10], abdominal surgeries [11], and thyroid operations [12]. Nevertheless, these surgeries were manually operated by surgeons, and their performance heavily depends on surgeons' clinical abilities and operational experiences [13]. To standardize general and tedious surgical subtasks and lesson surgeon fatigue in clinical surgery, autonomous manipulation through standard procedures should be further investigated.

To imitate the surgical task and eliminate large space consumptions [3], a robotic system usually consists of two robotic arms with grippers and a vision camera to provide hand-eye coordination as shown in Fig. 1. To evaluate 3-D positions of the grippers from the vision camera, Mayer and Parker [14] and El-Haddad and Tao [15] employed a stereo vision system, where 3-D positions can be evaluated through triangulation. Chu *et al.* [16] proposed an algorithm for evaluating the

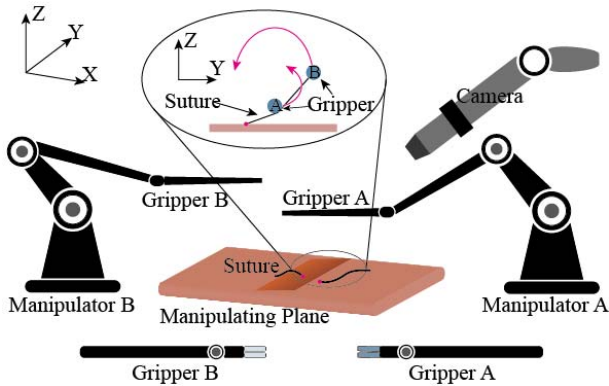


Fig. 1. Robotic system for surgical knot tying with two grippers to interact with the suture on the tissue surface.

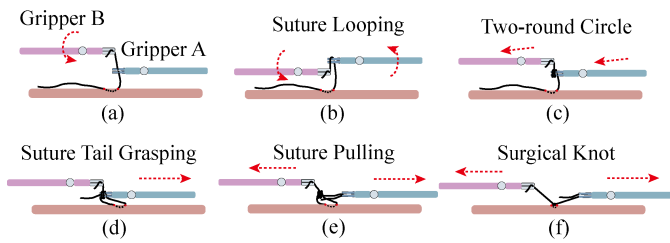


Fig. 2. General procedures of surgical knot tying. (a) Suture grasping. (b) and (c) Suture looping. (d) Suture tail grasping. (e) and (f) Suture pulling.

spatial position of a particular microobject from a single camera. The algorithm employed the image reflected from the surface as the additional feature for the evaluation. Espiau *et al.* [17] described another method for vision-based control in robotics, in which the proposed framework incorporated the visual system into the control loop to permit interactions between the robot and its surroundings. Putzer *et al.* [18] and Pyci'nski *et al.* [19] proposed the use of time-of-flight camera for navigating robots in a computer-aid surgery.

The instrument tie method is one of the common practices to tie a surgical knot [20] because of its ease of implementation. As illustrated in Fig. 2, the procedure consists of grasping the leading segment of the suture [Fig. 2(a)], wrapping two suture loops around a gripper [Fig. 2(b) and (c)], grasping the suture tail with another gripper [Fig. 2(d)], and pulling the suture to tighten the knot [Fig. 2(e) and (f)]. This method has been successfully implemented using laparoscopic [21] and other robot systems [5], [22], [23]. For instance, Croce [24] examined this instrument tie method and other methods that are suitable for laparoscopic surgery. Gopaldas and Reul [25] examined an alternative method to tie the knot, and the tool was manipulated to grasp the suture and rotated along its axle to form multiple suture loops. Guru *et al.* [26] proposed a novel robotic knot-tying technique that can be used for shorter suture length. The suture was manipulated to loop around the other end of the suture, rather than the gripper, to complete the knot. Muffly *et al.* [27] examined six-throw knot tying with da Vinci robot. Other common two-hand knot-tying techniques have also described in [28] and [29], which require higher dexterity from the manipulation tool.



Fig. 3. (a) and (b) Suture's slack and slippage while winding. (c) and (d) Collisions of the gripper with the suture.

A knot can be formed by using a fixture [30] or a unique tool [31] integrated at the end of the instrument. This knot-tying approach requires adding new hardware to the system, which may not be suitable for use in some surgical scenes. Autonomous knot tying can also be performed through learning from demonstration to establish statistical models [32]–[34]. For instance, Mayer *et al.* [35] proposed an autonomous approach for knot tying based on a single demonstration of the task with four robotic arms. Takamatsu *et al.* [36] presented a knot planning from observation paradigm, and a rope, rather than a suture thread, was examined in the experiment. Sen *et al.* [37] proposed a 3-D printed suture needle angle positioner as the tool, which can be combined with a sequential convex program to compute the needle path for multithrow surgical suturing.

Besides, trajectory-based tasks were also investigated in various operating environments. Nageotte *et al.* [38] employed kinematic analysis and geometric modeling to generate the path that can minimize the tissue deformation while driving the needle. DiMaio *et al.* [39] proposed a potential field-based path planning technique for needle placement and obstacle avoidance. Chow and Newman [22] examined a new knot-tying technique through roll-arc looping with the visual guidance.

The performance of knot tying through learning models heavily depend on the quality of training data, where a large amount of training data are usually hard to obtain due to privacy issue [40]. According to the studies, achieving high precision remains a challenging task [33], and failures were also observed in [35] and [37]. In contrast, path planning using trajectory equations is one of the simplest methods to generate the path based on the known information (map). This approach is comparable to road-map planning approach [41], but it can also handle constraints such as suture slippages, suture slacks, and equipment collisions, as illustrated in Fig. 3.

In this paper, we present a new robotic knot-tying technique that aims at reducing the workspace required to construct a surgical knot through simultaneous manipulation and coordination between two grippers. The 2-D spatial trajectories of grippers described in [42] were reformulated so that the decreasing rate of the suture length during the winding process was factored in the trajectory equations. The position offset along the center of axis direction was introduced

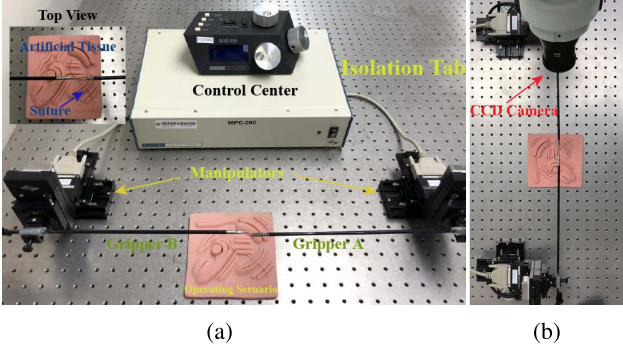


Fig. 4. Robotic system. (a) Overview. (b) Top view.

between the two grippers to facilitate the efficient formation of the suture loop. The proposed work shows advantages in workspace saving required as compared to [22], [29], and [43]. Different from Mayer's works using haptic sensors [4], [35], a simple in-house robotic system with a single camera was employed to compute the position information. This knot-tying method requires a manipulator with only three degrees of freedom (DOF) to perform and this method can be easily implemented using more sophisticated surgical robots.

Compared with [23], [35], and [44], this technique could also eliminate the need of adding markers on standard surgical instruments. The control scheme in [45] was further examined for visual servoing of the grippers. Derivations on the transformation between the image and the robot coordinates were provided and the accuracy in visual evaluation of the gripper position was examined through experiments. The control scheme was enhanced to handle object occlusion and new sets of experiments were conducted to evaluate the performance and robustness of the control scheme.

This paper is organized as follows. Section II introduces the experimental setup and the algorithm used in robotic knot tying. Section III describes the methodology for formulating the spatial trajectory planning for the suture looping task, the transformation matrix, and the dynamic control of the system. Section IV provides results and discussions on the robustness of the visual system and the performance of the automatic suture looping. A summary is given at the end of this paper.

II. OVERVIEW OF THE SYSTEM

A. Experimental Setups

The robotic system employed to conduct the experiment is shown in Fig. 4. Two laparoscopic grippers are attached to two motorized manipulators, MP-285, and these manipulators are connected to the MPC-200 controller. Each manipulator can provide three DOFs and the travel distance in every axis is 25 mm. In addition, a high-resolution camera is mounted on a stand to capture images in real time. The overall surgical task of knot tying is performed on an artificial tissue, and the system is configured on an antivibration table to isolate the disturbances from the surrounding environment.

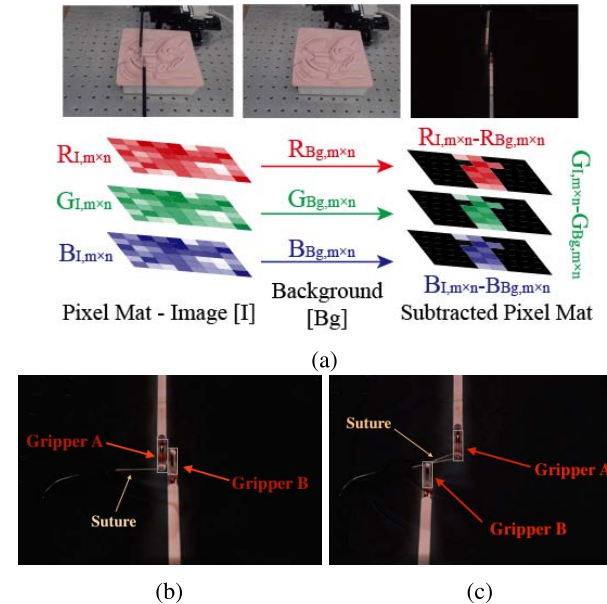


Fig. 5. Illustrations of the background subtraction algorithm and the object tracking. (a) Working principle of the background subtraction. (b) and (c) Two instances of the object tracking with the subtraction operation.

B. System Programming

A customized algorithm was developed to enable communications between the controller of the manipulators and the visual camera, which can guide the grippers to follow the planned trajectory for automated knot tying. The core parts of the program were outlined in Algorithm 1.

Algorithm 1 Object Detection

```

1 Capture the background image: mat  $\mathbb{B}_I \xrightarrow{\text{GaussianBlur}}$ 
   mat  $\mathbb{B}_I^G$ 
2  $\xrightarrow{\text{save}}$  filebackground
3 Truncate patterns of grippers: mat  $\mathbb{G}_A$  &  $\mathbb{G}_B \xrightarrow{\text{save}}$ 
   filepattern
4 for current camera image mat  $\mathbb{C}_I \xrightarrow{\text{GaussianBlur}}$  mat  $\tilde{\mathbb{C}}_I^G$ 
   do
5   mat  $\tilde{\mathbb{S}}_I^G \leftarrow \{\tilde{\mathbb{C}}_I^G - \mathbb{B}_I^G\}$  (subtraction)
6 end
7 Each searching point  $(x', y') \in \{\mathbb{G}_A \parallel \mathbb{G}_B\}$ 
8 for all  $(x_i, y_i) \in \tilde{\mathbb{S}}_I^G$  do
9   mat  $\mathbb{V}_{(x_i, y_i)} \leftarrow SQDIFFNORMED(x_i, y_i)$ 
10  =  $\frac{\sum_{(x', y')} [T(x', y') - I(x_i + x', y_i + y')]^2}{\sqrt{\sum_{(x', y')} T(x', y')^2 \cdot [\sum_{(x', y')} I(x_i + x', y_i + y')]^2}}$ 
11 end
12 Detected location:  $\mathcal{L}_{(x_d, y_d)} \leftarrow \text{argmin}\{\mathbb{V}_{(x_i, y_i)}\}$ 
13 Visualize detected positions of two grippers in GUI windows.

```

Precise evaluation of the gripper location $\mathcal{L}_{(x_L, y_L)}$ through the image could be influenced by environmental noises. To enhance the precision, a background subtraction method was adopted. First, an image of the surgical scene \mathbb{B}_I^G was captured, and two grippers were manipulated to the field for

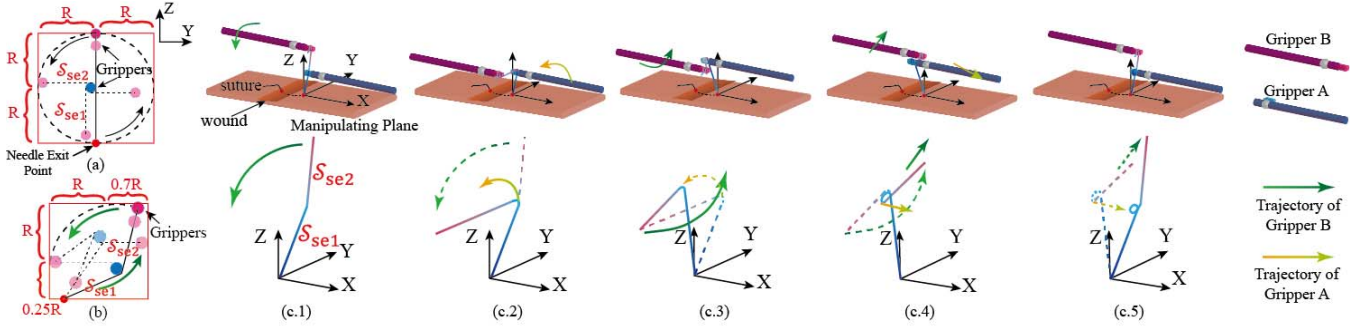


Fig. 6. 2-D sketch of the workspace using (a) traditional method and (b) proposed method. (c.1–c.5) Details of the proposed suture looping process at different key stages.

the operation. Fig. 5(a) shows the camera image, denoted as \mathbb{C}_I , before the operation. With this image as the reference, the background subtraction algorithm [46], [47] was employed to obtain the current image after subtraction as $\tilde{\mathbb{C}}_I^G$. Then, the template matching algorithm [48] was utilized and templates of the two grippers \mathbb{G}_A and \mathbb{G}_B were used to compute the correlation value $V_{(x_i, y_i)}$ at each image point (x_i, y_i) within the search area (x, y) . The locations with the highest correlation were identified as the grippers and their image coordinates were shown on the screen for visual monitoring in Fig. 5(b) and (c).

III. METHODOLOGY

To tie a surgical knot automatically with a robotic system, the procedure involves three main components: 1) generate a nonslipage and collision-free trajectory to dynamically construct the suture loops; 2) correlate the coordinates between the robot and the image frame; and 3) develop a control strategy to optimize the operational performance.

A. Spatial Trajectory Planning of Two Gitters

After a wound is stitched up with a suture, the first step to tie a surgical knot is to wrap the suture around a gripper (Gripper A) to form suture loops.

Conventionally [22], [29], [43], [49], the looping practice is to wind a full circle around an idle gripper as shown in Fig. 6(a), which consumes a large workspace. In contrast, our proposed approach revamps the practice by dynamically repositioning its center at different stages, as shown in Fig. 6(b).

The two grippers, initially at their respective positions with Gripper B grasping the leading segment of the suture, were manipulated to complete the suture winding as shown in Fig. 6(c.1)–(c.5). The lengths of two suture segments, between the needle exit point and Gripper A, S_{se1} , and between two grippers, S_{se2} , can be selected according to the size of the suture loop.

To complete a suture loop, five main stages were designed in our method. First, Gripper B moves along a semiround trajectory, centered by Gripper A, which was sketched in Fig. 6(c.1) and (c.2). In the second stage as shown in Fig. 6(c.3), centered at Gripper B, Gripper A circled up while keeping the suture

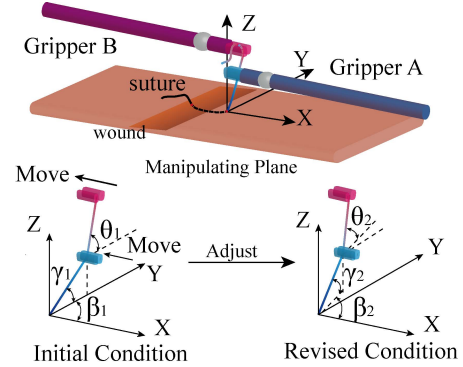


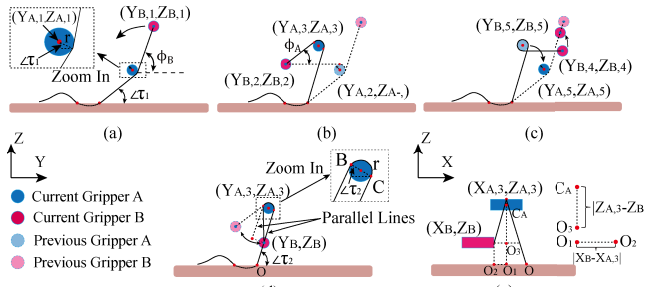
Fig. 7. Initial and revised orientations of the suture.

portions S_{se1} and S_{se2} in tension. Then, movements of Gripper B followed up, tracing a semiround trajectory that was centered at the new position of Gripper A, and reaching a height, at which S_{se2} was parallel to the manipulating plane. This process was sketched in Fig. 6(c.3) and (c.4). Next, Gripper A adjusted its position, and two grippers simultaneously moved and approximated their original locations. Finally, two grippers reached their destinations of the first loop. Following the same procedures, the second loop can be accomplished.

To eliminate suture slack and slippage as shown in Fig. 3(a) and (b), the grasped segment should be maintained vertical to the manipulating plane and kept in tension. Nevertheless, there is a possibility that Gripper B could collide with the suture segment S_{se1} near the needle exit point when constructing the loop, resulting in improper alignment in the x -direction as shown in Fig. 3(c) and (d). To avoid such problem, Gripper B with the grasped suture should be slightly moved along the x -axis to provide a clearance with respect to Gripper A.

In Fig. 7, the 3-D poses of the suture and the grippers were shown using angle notations. The angle between the projection of S_{se1} on the XY plane and the x -axis is defined as β , and the angle between S_{se2} and XY plane is defined as θ . Besides, γ indicates the angle between S_{se1} and XY plane.

The shifting in the x -axis can alter the angle β , and a proper displacement that ensures a sufficient clearance should be computed. Meanwhile, the incremental value of β should be maintained at a minimal level, which aims to prevent



the suture's creeping down the gripper's tip when winding. To make this looping process more reliable and convenient to be implemented, the planned trajectory was simplified as only moving in YZ -coordinates, and keeping X -coordinates of two grippers fixed. The locations of two grippers in the x -direction can be calculated using the following equations:

$$\begin{cases} x_A = S_{se1} \cdot \cos \gamma \cdot \cos \beta \\ x_B = S_{se1} \cdot \cos \gamma \cdot \cos \beta + S_{se2} \cdot \cos \theta \cdot \cos \beta. \end{cases} \quad (1)$$

To plan the reference trajectories, the 2-D sketches of the dominating looping motions in YZ plane were outlined in Fig. 8(a)–(c). The required trajectories of two grippers can be represented by a series of key points in YZ plane.

To begin planning the trajectory, different parameters can be figured out according to the size of the suture looping. For a 20-mm suture loop, S_{se1} , S_{se2} , θ are selected to be 20 mm, 21 mm, and 75° , respectively. The horizontal offset of Gripper A (H_A) is set as 5 mm and γ can be computed using $\arcsin(H_A/S_{se1})$. R_m is the length of the projection of S_{se2} in YZ plane, which can be computed as $R_m = ((S_{se2} \cdot \sin \theta)^2 + (S_{se2} \cdot \cos \theta \cdot \sin \beta)^2)^{1/2}$. r is the radius of Gripper A, which is equal to 2 mm. Φ_B is the dynamic angle of Gripper B in different sections, which denotes the angle between S_{se2} and y -axis in the 2-D situation as shown in Fig. 8(a). Similarly, Φ_A indicates the angle between S_{se1} and y -direction in the plane, which is shown in Fig. 8(b). The range for the two angles to travel at different stages are listed as $\Phi_{B,1 \Rightarrow 2} \in [\theta, \pi]$, $\Phi_{A,2 \Rightarrow 3} \in [0, \alpha = (\pi/4)]$, $\Phi_{B,3 \Rightarrow 4} \in [\alpha + \pi, 2\pi]$, and $\Phi_{A,4 \Rightarrow 5} \in [\pi, 11\pi/9]$. The needle exit point is the origin, and the planned paths of two grippers can be computed with the following equations:

$$\begin{cases} y_{B,1 \Rightarrow 2} = S_{se1} \cdot \cos \gamma \cdot \sin \beta \\ \quad + \left[R_m - \pi \cdot r \cdot \frac{\Phi_{B,1 \Rightarrow 2} - \theta}{\pi - \theta} \right] \cdot \cos(\Phi_{B,1 \Rightarrow 2}) \\ z_{B,1 \Rightarrow 2} = S_{se1} \cdot \sin \gamma + \left[R_m - \pi \cdot r \cdot \frac{\Phi_{B,1 \Rightarrow 2} - \theta}{\pi - \theta} \right] \\ \quad \cdot \sin(\Phi_{B,1 \Rightarrow 2}) \end{cases} \quad (2)$$

$$\begin{cases} y_{A,2 \Rightarrow 3} = y_{B,2} + (R_m - \pi \cdot r) \cdot \cos(\Phi_{A,2 \Rightarrow 3}) \\ \quad + r \cdot \sin(\Phi_{A,2 \Rightarrow 3}) \\ z_{A,2 \Rightarrow 3} = z_{B,2} + (R_m - \pi \cdot r) \cdot \sin(\Phi_{A,2 \Rightarrow 3}) \\ \quad - r \cdot \cos(\Phi_{A,2 \Rightarrow 3}) \end{cases} \quad (3)$$

$$\begin{cases} y_{B,3 \Rightarrow 4} = y_{A,3} + \left(R_m - 2\pi r \cdot \frac{\Phi_{B,3 \Rightarrow 4} - 2\alpha}{2\pi - 2\alpha} \right) \\ \quad \cdot \cos(\Phi_{B,3 \Rightarrow 4}) \\ z_{B,3 \Rightarrow 4} = z_{A,3} + \left(R_m - 2\pi r \cdot \frac{\Phi_{B,3 \Rightarrow 4} - 2\alpha}{2\pi - 2\alpha} \right) \\ \quad \cdot \sin(\Phi_{B,3 \Rightarrow 4}) \end{cases} \quad (4)$$

$$\begin{cases} y_{A,4 \Rightarrow 5} = y_{B,4} + (R_m - 2\pi \cdot r) \cdot \cos(\Phi_{A,4 \Rightarrow 5}) \\ z_{A,4 \Rightarrow 5} = z_{B,4} + (R_m - 2\pi \cdot r) \cdot \sin(\Phi_{A,4 \Rightarrow 5}) \end{cases} \quad (5)$$

where $y_{N,i \Rightarrow j}$ and $z_{N,i \Rightarrow j}$ denote the coordinates of Gripper N in y - and z -axes from stage (i) to stage (j). During the manipulation at each stage, only one gripper is moved and the other one remains stationary. When looping the suture around one gripper, the length of R_m was reduced continuously. This phenomenon was also taken into account in the trajectory equations to compute the gripper positions. The orientation angle β is essential to several parameters, including the minimal distance between the suture and the gripper as sketched in Fig. 8(d) and (e). Based on the required clearance of this minimal distance, the value of β can be figured out for the task. Therefore, the planned trajectories of grippers can be consequently generated using (1)–(5).

Robot-assisted looping process has been examined by a number of groups. In [43], an interchangeable end tool was employed to grasp the suture, which would increase the tool size and, hence, the possibility of collision between tools. In contrast, grippers with smaller tips are more dexterous to manipulate the suture. Murphy [29] proposed a theoretical analysis of square knot tying using the instrument tie method. In their work, only one gripper was used to wind the suture, and the other gripper remained stationary as shown in Fig. 6(a). Chow and Newman [22] proposed a “spiral rolling” method to manipulate the suture loop using one moving gripper. Comparing the workspace, the instrument tie method in Fig. 6(a) requires a workspace of $4R^2$ if assuming the length of S_{se1} and S_{se2} as R . In our approach, the required space is $2.125R^2$, which is only approximately 53% of the traditional method. The alternative “rolling arc looping” method proposed in [22] would even require nearly four times of the workspace as compared to our approach.

B. Computations of Transformation Matrix

Using a single camera, the visual information can be obtained, and the relationship between the image location and the robotic location of an object can be expressed as

$$\vec{g}_{N,i} = PRT \cdot \vec{g}_{N,R} \quad (6)$$

where $\vec{g}_{N,i} = [y_{N,i}, z_{N,i}, f]^T$ denotes the location of Gripper N in the image frame and $\vec{g}_{N,R} = [x_{N,R}, y_{N,R}, z_{N,R}, 1]^T$ indicates the coordinate of this gripper in the robot coordinate. Besides, we use $\vec{g}_{N,C} = [x_{N,C}, y_{N,C}, z_{N,C}, 1]^T$ to denote its location in the camera coordinate. R and T denote

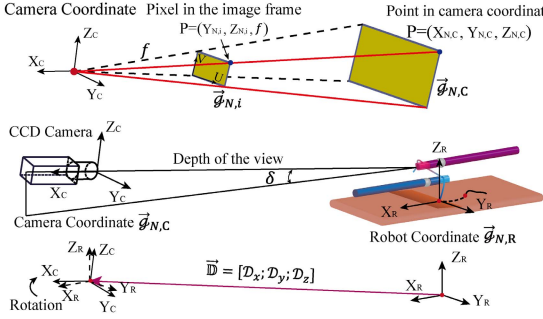


Fig. 9. Camera and robot coordinates of the visual system.

the rotational and the translational matrices required for the frame transformation, and P is the perspective transformation matrix [50]. The sketch of the visual system is shown in Fig. 9.

Similar to other visual servo systems, lens distortions were assumed to be negligible [51], [52], but serve distortion can be corrected through precalibration with chessboard images [53].

Based on the theory of the perspective projection, the correlation between the image frame and the camera coordinates can be calculated as

$$\frac{f}{x_{N,C}} = \frac{y_{N,i}}{y_{N,C} \cdot m} = \frac{z_{N,i}}{z_{N,C} \cdot m} \quad (7)$$

where m stands for the value (pixel/millimeters) between the image pixel and the camera coordinates, and f is the focal length of the camera. Using the homogeneous coordinates, the relationship between $\vec{g}_{N,i}$ and $\vec{g}_{N,C}$ can be derived as

$$\begin{bmatrix} y_{N,i}w \\ z_{N,i}w \\ w \end{bmatrix} = \underbrace{\text{diag}(mf, mf, 1)}_P \cdot \begin{bmatrix} 0 & 1 & 0 \\ 0 & 0 & 1 \\ 1 & 0 & 0 \end{bmatrix} \begin{bmatrix} x_{N,C} \\ y_{N,C} \\ z_{N,C} \end{bmatrix}. \quad (8)$$

With respect to the robot coordinates, the camera coordinates only rotates around the y -axis, and $\vec{D} = [D_x; D_y; D_z]$ denotes the displacement offsets between the camera frame and the robot frame. Thus, the ideal transformation matrix T_R^D can be expressed as

$$\begin{aligned} T_R^D &= R \cdot T \\ &= \begin{bmatrix} \cos \delta & 0 & \sin \delta & 0 \\ 0 & 1 & 0 & 0 \\ -\sin \delta & 0 & \cos \delta & 0 \\ 0 & 0 & 0 & 1 \end{bmatrix} \begin{bmatrix} 1 & 0 & 0 & D_x \\ 0 & 1 & 0 & D_y \\ 0 & 0 & 1 & D_z \\ 0 & 0 & 0 & 1 \end{bmatrix} \quad (9) \end{aligned}$$

where δ is the rotation angle of the y -axis. Thus, the relationship between $\vec{g}_{N,C}$ and $\vec{g}_{N,R}$ can be derived as

$$\begin{aligned} \begin{bmatrix} x_{N,C} \\ y_{N,C} \\ z_{N,C} \\ 1 \end{bmatrix} &= T_R^D \cdot \begin{bmatrix} x_{N,R} \\ y_{N,R} \\ z_{N,R} \\ 1 \end{bmatrix} \\ &= \begin{bmatrix} \cos \delta & 0 & \sin \delta & D_x \cdot \cos \delta + D_z \cdot \sin \delta \\ 0 & 1 & 0 & D_y \\ -\sin \delta & 0 & \cos \delta & -D_x \cdot \sin \delta + D_z \cdot \cos \delta \\ 0 & 0 & 0 & 1 \end{bmatrix} \begin{bmatrix} x_{N,R} \\ y_{N,R} \\ z_{N,R} \\ 1 \end{bmatrix}. \quad (10) \end{aligned}$$

Using (8)–(10), and letting $\mathcal{F} = m \cdot f$, the correlation between the image frame and the robot coordinates becomes

$$\begin{aligned} &\begin{bmatrix} y_{N,i}w \\ z_{N,i}w \\ w \\ 1 \end{bmatrix} \\ &= \begin{bmatrix} \mathcal{P} & \mathbf{0} \\ \mathbf{0} & 1 \end{bmatrix} \cdot T_R^D \cdot \mathcal{G}_{N,R} \\ &= \begin{bmatrix} 0 & \mathcal{F} & 0 & \mathcal{F} \cdot D_y \\ -\mathcal{F} \sin \delta & 0 & \mathcal{F} \cos \delta & -\mathcal{F} D_x \sin \delta + \mathcal{F} D_z \cos \delta \\ \cos \delta & 0 & \sin \delta & D_x \cos \delta + D_z \sin \delta \\ 0 & 0 & 0 & 1 \end{bmatrix} \\ &\times \begin{bmatrix} x_{N,R} \\ y_{N,R} \\ z_{N,R} \\ 1 \end{bmatrix}. \quad (11) \end{aligned}$$

Thus, the image location $[y_{N,i}, z_{N,i}]^T$ can be denoted as

$$\begin{aligned} y_{N,i} &= \frac{y_{N,R} \cdot \mathcal{F} + \mathcal{F} D_y}{x_{N,R} \cdot \cos \delta + z_{N,R} \cdot \sin \delta + D_x \cos \delta + D_z \sin \delta} \\ z_{N,i} &= \frac{-x_{N,R} \cdot \mathcal{F} \sin \delta + z_{N,R} \cdot \mathcal{F} \cos \delta - \mathcal{F} D_x \sin \delta + \mathcal{F} D_z \cos \delta}{x_{N,R} \cdot \cos \delta + z_{N,R} \cdot \sin \delta + D_x \cos \delta + D_z \sin \delta}. \quad (12) \end{aligned}$$

In a fixed visual system, the displacement vector \vec{D} between the camera and the robot shown in Fig. 9 should be constant. To loop the suture, two grippers do not involve movements in the X -coordinate and, hence, $x_{N,R}$ is a constant. Owing to the large depth of the visual system, the small tilt angle δ becomes negligible and can be approximated as zero. Thus, for both grippers, $z_{N,R} \cdot \sin \delta \approx 0$, and $(x_{N,R} \cdot \cos \delta + D_x \cos \delta + D_z \sin \delta)$ can be regarded as a constant. Therefore, the denominators of $y_{N,i}$ and $z_{N,i}$ can be regarded as a constant \mathbb{C}_1 . Besides, $(-x_{N,R} \cdot \mathcal{F} \sin \delta - \mathcal{F} D_x \sin \delta) \approx 0$. Thus, (12) can be further derived as

$$\begin{cases} y_{N,i} = \frac{\mathcal{M}_{11} \cdot y_{N,R} + \mathcal{M}_{12} \cdot z_{N,R} + \mathbb{C}_2}{\mathbb{C}_1} \\ z_{N,i} = \frac{\mathcal{M}_{21} \cdot y_{N,R} + \mathcal{M}_{22} \cdot z_{N,R} + \mathbb{C}_3}{\mathbb{C}_1} \end{cases} \quad (13)$$

where $\mathbb{C}_1 = x_{N,R} \cdot \cos \delta + D_x \cdot \cos \delta$, $\mathbb{C}_2 = \mathcal{F} D_y$, $\mathbb{C}_3 = \mathcal{F} D_z \cdot \cos \delta$, $\mathcal{M}_{11} = \mathcal{F}$, $\mathcal{M}_{22} = \mathcal{F} \cdot \cos \delta$, and $\mathcal{M}_{12} = \mathcal{M}_{21} = 0$. Equation (13) can be expressed as

$$\begin{bmatrix} y_{N,i} \\ z_{N,i} \end{bmatrix} = \begin{bmatrix} \mathcal{M}_{11}/\mathbb{C}_1 & \mathcal{M}_{12}/\mathbb{C}_1 \\ \mathcal{M}_{21}/\mathbb{C}_1 & \mathcal{M}_{22}/\mathbb{C}_1 \end{bmatrix} \begin{bmatrix} y_{N,R} \\ z_{N,R} \end{bmatrix} + \begin{bmatrix} \mathbb{C}_2/\mathbb{C}_1 \\ \mathbb{C}_3/\mathbb{C}_1 \end{bmatrix} \quad (14)$$

which can be further derived as

$$\begin{bmatrix} y_{N,R} \\ z_{N,R} \end{bmatrix} = \begin{bmatrix} \mathcal{M}_{11}/\mathbb{C}_1 & \mathcal{M}_{12}/\mathbb{C}_1 \\ \mathcal{M}_{21}/\mathbb{C}_1 & \mathcal{M}_{22}/\mathbb{C}_1 \end{bmatrix}^{-1} \left\{ \begin{bmatrix} y_{N,i} \\ z_{N,i} \end{bmatrix} - \begin{bmatrix} \mathbb{C}_2/\mathbb{C}_1 \\ \mathbb{C}_3/\mathbb{C}_1 \end{bmatrix} \right\}. \quad (15)$$

With these derived results, it can be updated that $\vec{g}_{N,i} = [(y_{N,i}), (z_{N,i})]^T$. Since the X -coordinates were fixed, grippers' motion $\vec{g}_{N,R}$ can be simplified to the 2-D condition

as $[(y_{N,R}, z_{N,R})]^T$. Besides, $\vec{\mathcal{O}}_N = [\mathbb{C}_2/\mathbb{C}_1, \mathbb{C}_3/\mathbb{C}_1]^T$, and $\mathcal{T}_N = \begin{bmatrix} \mathcal{M}_{11}/\mathbb{C}_1 & \mathcal{M}_{12}/\mathbb{C}_1 \\ \mathcal{M}_{21}/\mathbb{C}_1 & \mathcal{M}_{22}/\mathbb{C}_1 \end{bmatrix}$. Thus, the relationship between the position in the image frame and the YZ position in the robot coordinates of Gripper N can be expressed as

$$\vec{\mathcal{G}}_{N,R} = \mathcal{T}_N(\vec{\mathcal{G}}_{N,i} - \vec{\mathcal{O}}_N) \quad (16)$$

where $\vec{\mathcal{O}}_N$ can be used to denote the offset between the origin of the image frame and the projection of the robot coordinate's origin in this frame. This value can also be computed in the calibration process and denoted as $(y_{N,i}^*, z_{N,i}^*)$.

Since evaluating cameras' intrinsic parameters are time consuming, and the relationship between $\vec{\mathcal{G}}_{N,R}$ and $\vec{\mathcal{G}}_{N,i}$ can be derived as in the form of (16), the transformation matrix \mathcal{T}_N used to map the relationship between $\vec{\mathcal{G}}_{N,R}$ and $\vec{\mathcal{G}}_{N,i}$ can be computed using an experimental approach through the least-squares estimation method in [54], and the equation can be expressed as

$$\mathcal{T}_N = (G_{N,R}) \cdot (G_{N,i})^T \cdot [(G_{N,i}) \cdot (G_{N,i})^T]^{-1}. \quad (17)$$

To calculate this \mathcal{T}_N in the calibration process, the gripper was commanded to K points in the workspace, and K groups of image coordinates $(\vec{\mathcal{G}}_{N,i})_{PK} = [(y_{N,i})_{PK}, (z_{N,i})_{PK}]$ can be obtained using Algorithm 1, and their respective robot coordinates, $(\vec{\mathcal{G}}_{N,R})_{PK} = [(y_{N,R})_{PK}, (z_{N,R})_{PK}]$, can also be acquired through the motor encoders of the manipulators.

The detailed expressions of $G_{N,i}$ and $G_{N,R}$ were listed in (18), as shown at the bottom of the next page. Using this method, the transformation relationship can be quickly constructed without investigating the intrinsic parameters using this experimental calibration approach.

C. Optimal Control Scheme

In this paper, two grippers were required to follow the planned trajectories to complete the suture loop. To account for uncertainties or impulse disturbances in manipulation, a controller with visual feedback was added to the robotic system to enhance the performance of driving grippers.

Since targets of planned trajectory were time variant, the linear quadratic (LQ) controller was implemented because it could minimize the one-step delay by computing the input that could optimize the error at the next step when tracking moving objects, and consequently improve the robustness of the operation. Besides, the LQ controller was adopted because it is simple design and it can be conveniently implemented in general vision-based systems.

For an input $\vec{u}_N(n)$ of Gripper N, the desired position at the next time step ($n+1$) can be computed in the state-space form as

$$\vec{\mathcal{G}}_{N,R}(n+1) = \vec{\mathcal{G}}_{N,R}(n) + \mathcal{B}(n) \cdot \vec{u}_N(n) \quad (19)$$

where $\mathcal{B}(n)$ is the coefficient matrix of the input. $\vec{\mathcal{P}}_{N,R}$ is employed to denote the planned trajectory.

The strategy [55], [56] in designing the LQ controller was to minimize a cost function that placed a cost on the error between the real position and planned position of grippers in

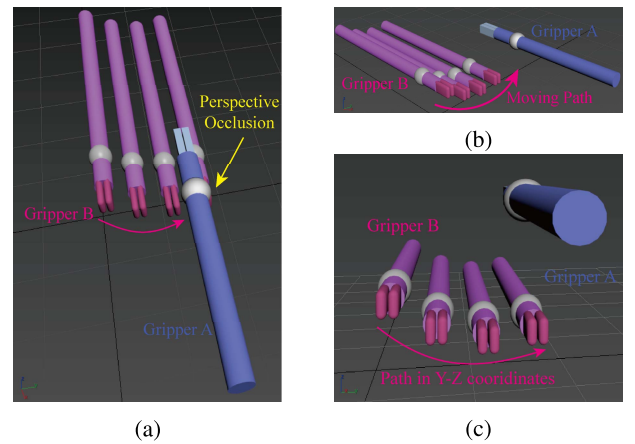


Fig. 10. Occlusions of grippers during the suture looping procedure. (a) Perspective occlusion of gripper B. (b) and (c) Moving trajectory of gripper B.

the next time step, $[\vec{\mathcal{G}}_{N,R}(n+1) - \vec{\mathcal{P}}_{N,R}(n+1)]$, and a cost on the control input $\vec{u}_N(n)$. The cost function is

$$\begin{aligned} E(n+1) = & [\vec{\mathcal{G}}_{N,R}(n+1) - \vec{\mathcal{P}}_{N,R}(n+1)]^T \cdot \mathcal{Q} \\ & \cdot [\vec{\mathcal{G}}_{N,R}(n+1) - \vec{\mathcal{P}}_{N,R}(n+1)] \\ & + \vec{u}_N^T(n) \cdot \mathcal{L} \cdot \vec{u}_N(n) \end{aligned} \quad (20)$$

where \mathcal{Q} and \mathcal{L} are the weighting matrices. Substituting (19) into (20) yields

$$\begin{aligned} E(n+1) = & [\vec{\mathcal{G}}_{N,R}(n) + \mathcal{B}(n) \cdot \vec{u}_N(n) - \vec{\mathcal{P}}_{N,R}(n+1)]^T \\ & \cdot \mathcal{Q} \cdot [\vec{\mathcal{G}}_{N,R}(n) + \mathcal{B}(n) \cdot \vec{u}_N(n) - \vec{\mathcal{P}}_{N,R}(n+1)] \\ & + \vec{u}_N^T(n) \cdot \mathcal{L} \cdot \vec{u}_N(n). \end{aligned} \quad (21)$$

By differentiating (21) with respect to $\vec{u}_N(n)$, and setting the gradient of the error term to zero [57], the optimal control input $\vec{u}_N(n)$ can be calculated as

$$\begin{aligned} \vec{u}_N(n) = & -[\mathcal{B}^T(n) \cdot \mathcal{Q} \cdot \mathcal{B}(n) + \mathcal{L}]^{-1} \cdot \mathcal{B}^T(n) \cdot \mathcal{Q} \\ & \cdot \underbrace{[\mathcal{T}_N \cdot (\vec{\mathcal{G}}_{N,i}(n) - \vec{\mathcal{O}}) - \vec{\mathcal{P}}_{N,R}(n+1)]}_{\text{error}}. \end{aligned} \quad (22)$$

Two weighting matrices, \mathcal{Q} and \mathcal{L} , can provide tunability on the system performance by setting more or less emphasis on the error of the gripper's motion and on the control input, respectively. Here, these two matrices were chosen to be scalar matrices to set equal weighting on the entry for each axis as

$$\mathcal{Q} = \mathcal{T}_1 \cdot I \quad \mathcal{L} = \mathcal{T}_2 \cdot I \quad (23)$$

where I is an identity matrix, and \mathcal{T}_1 and \mathcal{T}_2 are the tuning parameters of \mathcal{Q} and \mathcal{L} , respectively. Different values for \mathcal{T}_1 and \mathcal{T}_2 should be evaluated through tests to determine the optimal pairs for the tracking task. After system tuning, the computed input $\vec{u}_N(n)$ was sent to the micromanipulators to drive the grippers accordingly.

D. Estimation of Lost Track Point

When using visual images for control purpose, image occlusion could lead to unstable or lose track of target when using

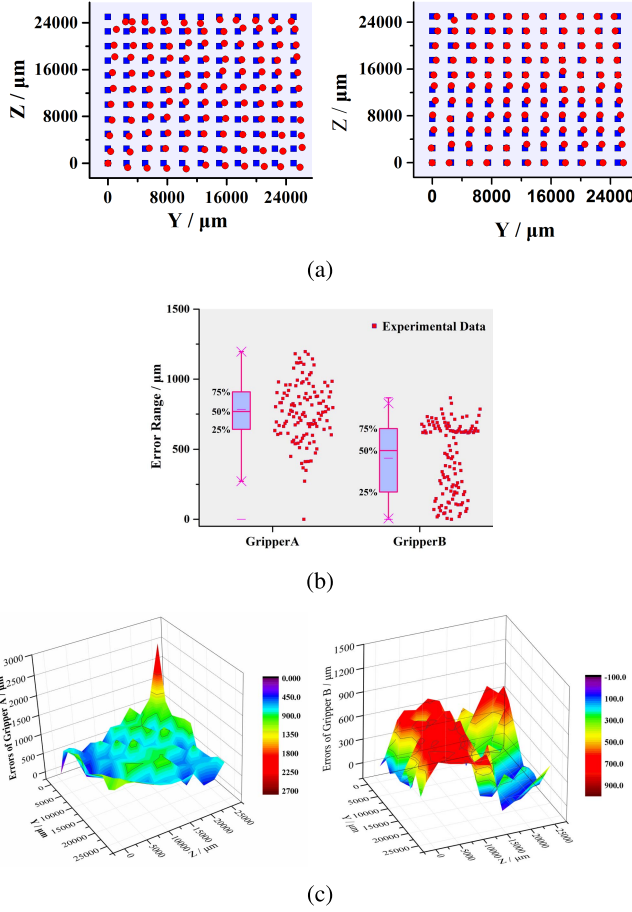


Fig. 11. Test results of the visual servoing system. (a) Planned and calculated positions of two grippers in YZ -coordinates. (b) Box chart of test error results. (c) Errors between planned and calculated locations of two grippers at testing points.

the pattern matching algorithm, resulting errors in computing the control inputs. In this paper, Gripper B could be temporarily blocked by Gripper A when winding the suture in stage three, as sketched in Fig. 10(a).

In this situation, the false detection of the gripper position may occur, and improper information could be fed to the controller, resulting a severe error in positioning the gripper in the next interval. To resolve the occlusion problem, the posi-

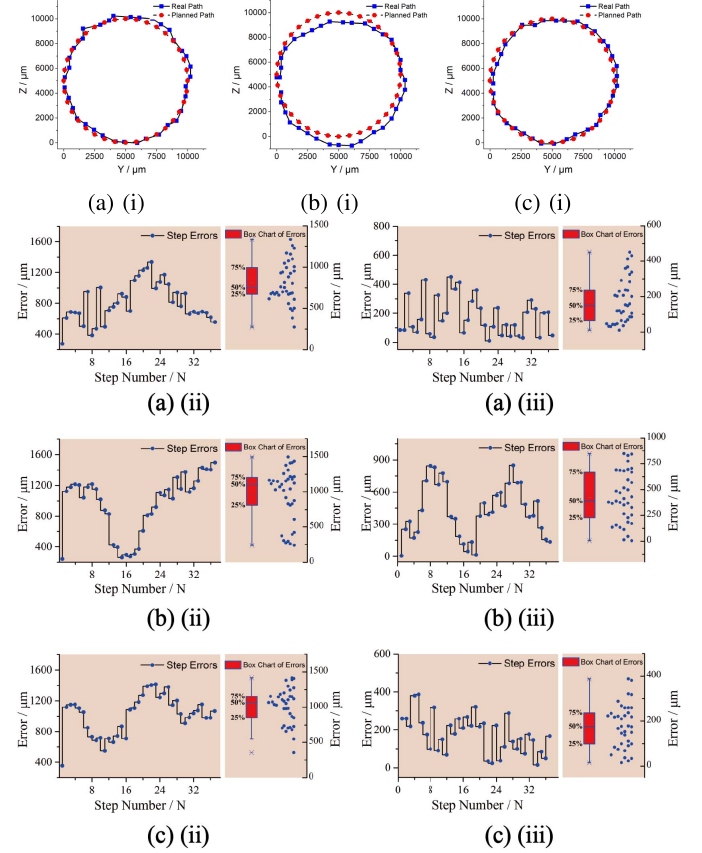


Fig. 12. (a)–(c) Experimental results from three trials using: $T_1 = 3$, $T_2 = 0.2$, and radius = $5000 \mu\text{m}$. (i) Planned and real trajectories of the gripper. (ii) Time-dependent step errors of the gripper. (iii) Time-Independent step errors of the gripper.

tion of the corresponding gripper will be substituted by an estimated position when lost track occurs.

During the manipulation, the gripper could be blocked at the t th time step. This kind of lost tracking phenomenon is not common in the knot tying and it may only happen in two or three times. As illustrated in Fig. 10(b) and (c), the path of the occluded gripper was sketched. The planned 2-D trajectory in this period was similar to a second-order polynomial curve. Using the information in previous ε steps,

$$\begin{aligned}
 G_{N,i} &= \left\{ \begin{array}{ll} [(y_{N,i})_{\mathcal{P}1} - (y_{N,i})^*] - \frac{1}{K} \sum_{j=1}^K [(y_{N,i})_{\mathcal{P}j} - (y_{N,i})^*] & \dots \quad [(y_{N,i})_{\mathcal{P}K} - (y_{N,i})^*] - \frac{1}{K} \sum_{j=1}^K [(y_{N,i})_{\mathcal{P}j} - (y_{N,i})^*] \\ [(z_{N,i})_{\mathcal{P}1} - (z_{N,i})^*] - \frac{1}{K} \sum_{j=1}^K [(z_{N,i})_{\mathcal{P}j} - (z_{N,i})^*] & \dots \quad [(z_{N,i})_{\mathcal{P}K} - (z_{N,i})^*] - \frac{1}{K} \sum_{j=1}^K [(z_{N,i})_{\mathcal{P}j} - (z_{N,i})^*] \end{array} \right\} \\
 G_{N,R} &= \left\{ \begin{array}{ll} (y_{N,R})_{\mathcal{P}1} - \frac{1}{K} \sum_{j=1}^K [(y_{N,R})_{\mathcal{P}j}] & (y_{N,R})_{\mathcal{P}2} - \frac{1}{K} \sum_{j=1}^K [(y_{N,R})_{\mathcal{P}j}] \quad \dots \quad (y_{N,R})_{\mathcal{P}K} - \frac{1}{K} \sum_{j=1}^K [(y_{N,R})_{\mathcal{P}j}] \\ (z_{N,R})_{\mathcal{P}1} - \frac{1}{K} \sum_{j=1}^K [(z_{N,R})_{\mathcal{P}j}] & (z_{N,R})_{\mathcal{P}2} - \frac{1}{K} \sum_{j=1}^K [(z_{N,R})_{\mathcal{P}j}] \quad \dots \quad (z_{N,R})_{\mathcal{P}K} - \frac{1}{K} \sum_{j=1}^K [(z_{N,R})_{\mathcal{P}j}] \end{array} \right\} \quad (18)
 \end{aligned}$$

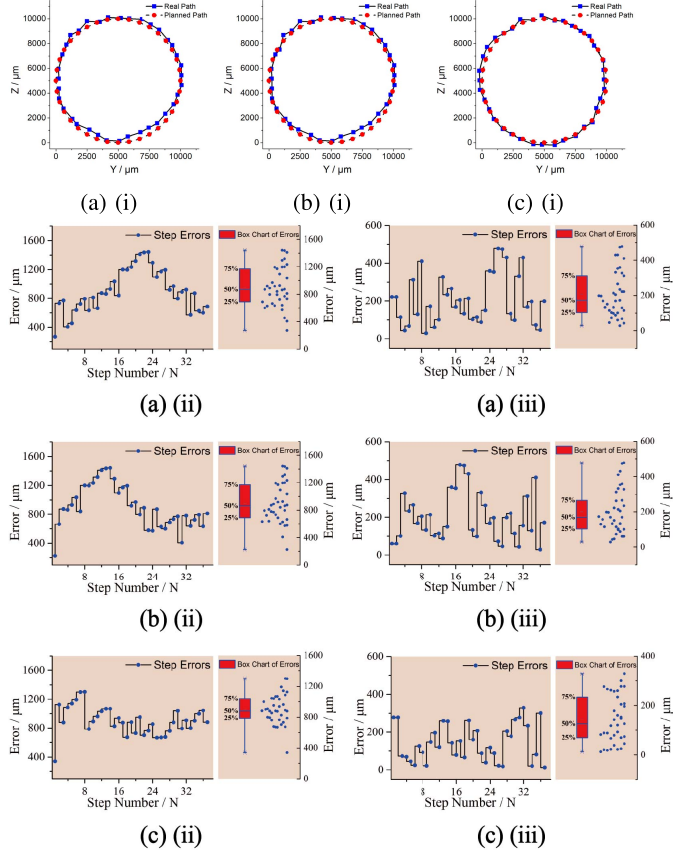


Fig. 13. (a)–(c) Experimental results from three trials using: $\mathcal{T}_1 = 5$, $\mathcal{T}_2 = 0.1$, and radius = 5000 μm . (i) Planned and real trajectories of the gripper. (ii) Time-dependent step errors of the gripper. (iii) Time-independent step errors of the gripper.

the prediction model can be established as

$$\vec{\mathcal{G}}_{N,R}(t - \varepsilon|t - 1) = S_{t-\varepsilon|t-1} \cdot J_{t-1} \quad (24)$$

where $\vec{\mathcal{G}}_{N,R}(t - \varepsilon|t - 1)$ denotes the matrix containing the information of gripper positions in the previous ε steps, $S_{t-\varepsilon|t-1}$ is the time step matrix, and J_{t-1} denotes the parameters of the estimation model, which can be computed as

$$J_{t-1} = \begin{bmatrix} j_{11} & j_{12} \\ j_{21} & j_{22} \\ j_{31} & j_{32} \end{bmatrix}_{t-1} = \begin{bmatrix} S_{t-\varepsilon}^2 & S_{t-\varepsilon} & 1 \\ S_{t-\varepsilon+1}^2 & S_{t-\varepsilon+1} & 1 \\ \dots & \dots & \dots \\ S_{t-1}^2 & S_{t-1} & 1 \end{bmatrix}^{-1} \cdot \begin{bmatrix} y_{N,R}(t - \varepsilon) & z_{N,R}(t - \varepsilon) \\ y_{N,R}(t - \varepsilon + 1) & z_{N,R}(t - \varepsilon + 1) \\ \dots \\ y_{N,R}(t - 1) & z_{N,R}(t - 1) \end{bmatrix}. \quad (25)$$

The matrix J_t will iteratively updated at each time interval t . Thus, the occluded position $\hat{\vec{\mathcal{G}}}_{N,R}(t)$ can be estimated as

$$\hat{\vec{\mathcal{G}}}_{N,R}(t) = S_t \cdot J_{t-1}. \quad (26)$$

If successive occlusions happen in the manipulation, the prepredicted locations can be taken as the input, and iteratively update the model parameters. The general procedures of our control scheme were summarized in Algorithm 2.

Algorithm 2 General Procedures of the Control Scheme

```

1   for each loop  $n$  do
2     After driven by  $\vec{\mathcal{G}}_{N,R}(n)$ 
3      $\vec{\mathcal{G}}_{N,i}(n) \leftarrow$  Algorithm 1
4     if (GripperN  $\leftarrow$  Not Occlusion)
5        $\vec{\mathcal{G}}_{N,R}(n) = T_N \cdot [\vec{\mathcal{G}}_{N,i}(n) - \vec{\mathcal{O}}_N]$ 
6     end
7     if (GripperN  $\leftarrow$  Occlusion)
8        $\hat{\vec{\mathcal{G}}}_{N,R}(n) = S_t \cdot S_{n-\varepsilon|n-1}^{-1} \cdot \vec{\mathcal{G}}_{N,R}(n - \varepsilon|n - 1)$ 
9     end
10     $\vec{u}_N(n) \xleftarrow{\text{LQ Controller}} \{\vec{\mathcal{G}}_{N,R}(n), \vec{\mathcal{P}}_{N,R}(n + 1)\}$ 
11     $\vec{\mathcal{G}}_{N,R}(n + 1) \xleftarrow{\text{Send}} \{\vec{\mathcal{G}}_{N,R}(n), \vec{u}_N(n)\}$  (Eq. 19 and 22)
12    Manipulator  $\xleftarrow{\text{Send}} \vec{\mathcal{G}}_{N,R}(n + 1)$ 
13  end

```

IV. EXPERIMENTAL RESULTS OF ROBOTIC KNOT TYING

A. Accuracy Tests of the Visual System

The automated process of the knot tying relies on visual feedback to compute the control inputs for task executions. Hence, it is important to ensure the accuracy of the vision-based evaluation method.

Prior to the knot-tying operation, the gripper was first manipulated to the lower left corner of the camera frame and this position was taken as the initial position. Then, this gripper was moved at an increment of 2.5 mm along the y - and z -directions to reach different points in the YZ plane. Image coordinates of the gripper were evaluated and transformed back to the robot coordinates for comparison with the theoretical values from the encoder. A set of 121 points were collected and results were summarized in Fig. 11(a). The manipulating errors between the vision-based computed values and the input values were also computed and plotted in Fig. 11(b).

It is noticed that the evaluation method provides comparable results on both grippers. The average errors of Gripper A and Gripper B were 0.78 and 0.43 mm, respectively, and the largest error of two grippers was less than 1.25 mm. Besides, from the analysis of the standard deviations of all these data, error tolerances of two grippers were 0.78 ± 0.26 mm and 0.43 ± 0.25 mm. Considering our experimental setup that has a $25 \text{ mm} \times 25 \text{ mm}$ plane workspace, the maximum values of tolerances 1.04 and 0.68 mm can be regarded as acceptable. Setting the bigger tolerance value as the threshold, for all 242 testing points, only 30 of them exceeded this limit.

It is also intuitively noticed from Fig. 11(c) that large errors of Gripper A occurred when the position approached the image corner. The main reason might result from the camera distortion at the boundary, but the overall performance and accuracy of the object detection algorithm were proven to be effective for this suture looping task.

B. Selections of Tuning Parameters

In Section III-C, it was clarified that \mathcal{Q} and \mathcal{L} should be properly selected by tuning \mathcal{T}_1 and \mathcal{T}_2 . To determine the optimal values for the tuning parameters in the LQ controller,

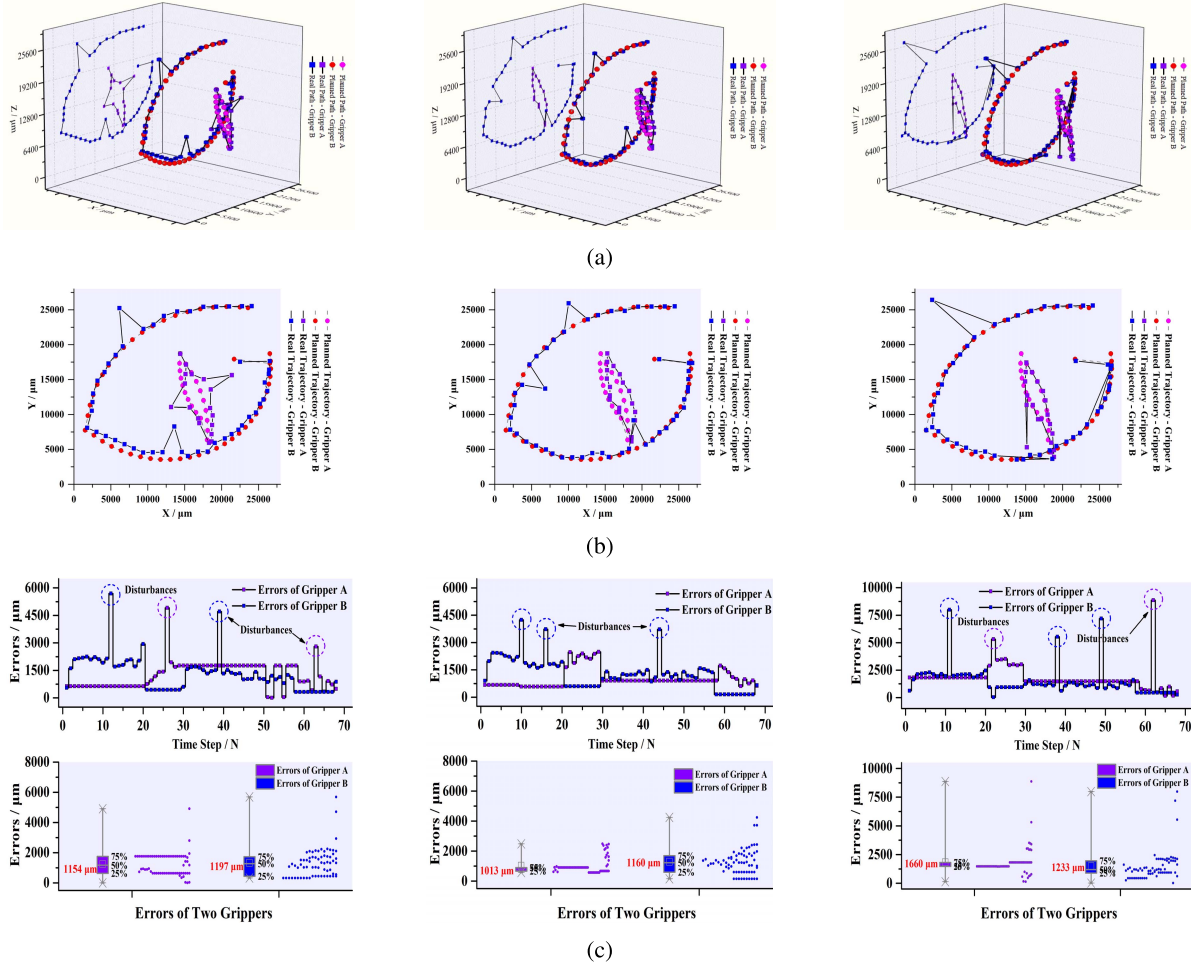


Fig. 14. Experimental results of suture looping under external impulse disturbances. $\mathcal{T}_1 = 5$ and $\mathcal{T}_2 = 0.1$, unit: micrometers. (a) Planned and real spatial trajectories of two grippers, with trajectory projection in YZ plane. (b) Planned and real trajectories of two grippers in YZ -coordinates. (c) Step errors via time steps of two grippers under impulse disturbances.

one gripper was commanded to move along a round trajectory with a radius of 5 mm, and tracking performances with different tuning parameters were examined.

For the first set of the tuning parameters, three trials were conducted and the results were shown in Fig. 12. It was observed that the gripper can successfully follow the planned path in all three trials. Errors between real positions and planned positions in each time step can be treated as the time-dependent errors. They were sketched in Fig. 12(a-ii), (b-ii), and (c-ii). The average value of them was 0.92 mm.

Referring to the time-independent errors, which can be calculated as the shortest distance between the real trajectories and the standard circle, their values were plotted in Fig. 12(a-iii), (b-iii), and (c-iii). These outcomes revealed the deviations between the planned and the real trajectories. The average value of these time-independent errors was calculated as 0.26 mm.

From this group, server errors can be noticed, especially in the second trial. In this regard, the second set of parameters aiming to reduce these instabilities was selected. We increased the value of \mathcal{T}_1 , and decreased the value of \mathcal{T}_2 . Similarly, three trials were carried out and the results were shown in Fig. 13.

As expected, the gripper can still successfully follow the planned trajectory. Comparing to the first group, the average

values of the time-dependent and time-independent errors were reduced to 0.89 and 0.18 mm, respectively. The decrease of the time-independent error showed an improvement of the control scheme in the trajectory tracking performance. The error values tend to be steadier as compared with the previous group.

Different \mathcal{T}_1 and \mathcal{T}_2 were also examined, but there were no obvious improvements in the tracking performance. To avoid the over-tuning, $\mathcal{T}_1 = 5$ and $\mathcal{T}_2 = 0.1$ were selected.

C. Control Scheme Under External Impulse Disturbances

The robustness of the LQ control method is another vital element in automated RAS. External disturbances might happen in the surgery, and they could be applied to grippers as sudden impulses. To emulate such effect, biases were randomly exerted to the grippers and the response of the control scheme was evaluated.

During the test, grippers were commanded to construct loops without the suture by following the planned trajectory. Random biases were added to the gripper original inputs, which shifted the grippers away from their planned positions. A total of 12 disturbances were added throughout the whole trajectories. With fixed X -coordinates, three

TABLE I

MEAN VALUES OF TIME-DEPENDENT ERRORS ($\mathcal{T}_1 = 5$ AND $\mathcal{T}_2 = 0.1$ UNIT: MICROMETERS)

Experiment Number	Group 1	Group 2	Group 3
Gripper A	1154	1013	1660
Gripper B	1197	1160	1233



Fig. 15. Lost tracking of grippers in the suture looping process.

groups of the planned and the real trajectories were sketched in Fig. 14(a). The corresponding paths in YZ plane were shown in Fig. 14(b), and the error analysis was shown in Fig. 14(c).

It can be noticed the LQ controller can quickly respond to such deviations and guide the gripper back to the planned trajectory. Since the targets are moving over time, prompt reaction to such sharp biases fully satisfies the requirements of the dynamic task, which can minimize influence from external disturbances and ensure the safety of the wound suturing.

The average values concerning the time-dependent errors of the two grippers were computed and listed in Table I. Referring to these results, they were within the range between 1.0 and 1.7 mm.

D. Estimations of the Lost Track Points

Occlusions due to the presence of one gripper could result in the lost track of another gripper's position in the image frame as mentioned in Section III-C.

During the operation, Gripper B might be occluded by Gripper A as shown in Fig. 15. To resolve such problem, a second-order prediction model was established. Four groups of tests were conducted to validate the feasibility of the approach.

In the first two groups, there were no occlusions during the looping procedure, but we assumed that the visual system could not detect the position of Gripper B at some certain time steps. Hence, the prediction model could be employed to calculate its location. Treating the real locations as the ground truth, and comparing with the predicted ones, the accuracy of the prediction model could be preliminarily evaluated. The results of Group 1 and 2 were shown in Fig. 16. The prediction model was generated using the data from the previous six steps, and the parameters of these two models were listed in Table II.

In Fig. 16, the estimated YZ -coordinates, as well as the step errors of Gripper B at the certain time step were indicated. The step errors were 950.1 and 579.9 μm . Comparing to the ground truth, errors between the predicted points and the real ones were only 595.3 and 390.4 μm , which were acceptable in our task.

TABLE II

PARAMETERS OF J —GROUP 1 AND GROUP 2

Group 1		Group 2	
j_{11} 35.18	j_{12} 100.29	j_{11} -32.59	j_{12} 76.86
j_{21} -1494.3	j_{22} -7668.3	j_{21} 3672.1	j_{22} -6017.1
j_{31} 18578	j_{32} 150699	j_{31} -79087	j_{32} 121511
Errors compared with planned positions $\vec{P}_{N,R}$		$950.1 \mu\text{m}$ $579.9 \mu\text{m}$	
Errors compared with real positions $\vec{G}_{N,R}$		$595.3 \mu\text{m}$	$390.4 \mu\text{m}$

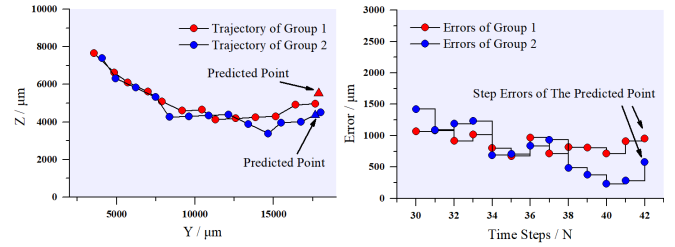


Fig. 16. Trajectories of gripper B, comparison between the predicted and real points.

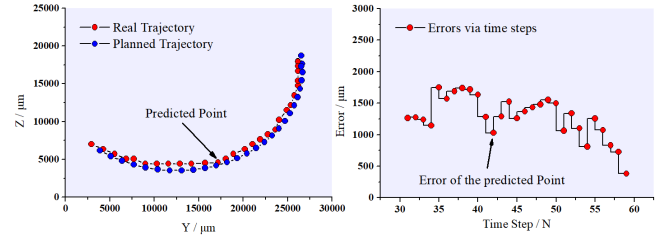


Fig. 17. Predicted location, real, and planned trajectories of the gripper, and errors at each time step—Group 3.

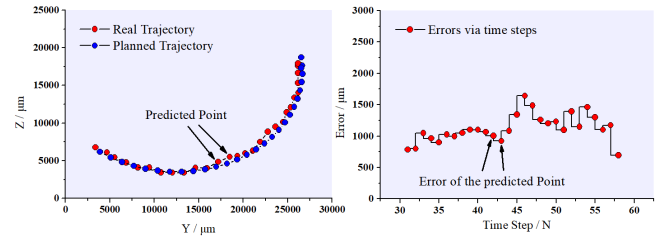


Fig. 18. Predicted location, real, and planned trajectories of the gripper, and errors at each time step—Group 4.

In Group 3, experiments with the real lost track scenario when looping the suture were examined. By employing the prediction model, the position of the lost track could be computed. In Fig. 17, the lost position was figured out, and it was noticed the predicted point could be smoothly fit into the entire trajectory. Besides, the parameters of the prediction model were listed in Table III, and the step error of the



Fig. 19. Snapshots of the suture looping procedure—captured from the charge-coupled device camera frame.

TABLE III
PARAMETERS OF J —GROUPS 3 AND 4

Group 3		Group 4			
		Model 1		Model 2	
j_{11}	j_{12}	j_{11}	j_{12}	j_{11}	j_{12}
23.21	8.75	-0.73	104.79	-0.51	75.71
j_{21}	j_{22}	j_{21}	j_{22}	j_{21}	j_{22}
-456.4	-659.5	1350.2	-8027.1	1332.4	-5707.2
j_{31}	j_{32}	j_{31}	j_{32}	j_{31}	j_{32}
-4637	16840	-38222	157155	-37867	110944
Errors compared with planned positions $\vec{P}_{N,R}$					
1027.3 μm		1005.4 μm		922.5 μm	

lost track point was computed as 1027.3 μm , which was maintained at a stable level.

In Group 4, successive occlusions happened in the manipulation when Gripper B was occluded in the camera frame at two continuous steps. To figure out the first lost track point, the prediction model was adopted. Treating the first predicted location as an input, the prediction model can be iteratively updated to estimate the second lost track point.

The parameters of prediction models in two successive occlusions were also listed in Table III, with these online computer models, the lost track coordinates were figured out and shown in Fig. 18. Two predicted locations were smoothly fit into the overall trajectory, and the time-dependent errors were 1005.4 and 922.5 μm , respectively, which were also illustrated in the figure. It could be noticed there were no abrupt increase in the error during the manipulation, and their magnitude was maintained at a stable level, which revealed that the proposed scheme was robust to internal and external errors.

E. Experimental Results of the Suture Looping

Finally, the complete suture looping process was examined with a suture on an artificial tissue. The suture was stitched through the wound on the tissue, and Gripper B was manipulated to grasp the suture's leading segment. Gripper A was positioned with respect to the needle exit point, and trajectories were generated using (1)–(5). Combining with the

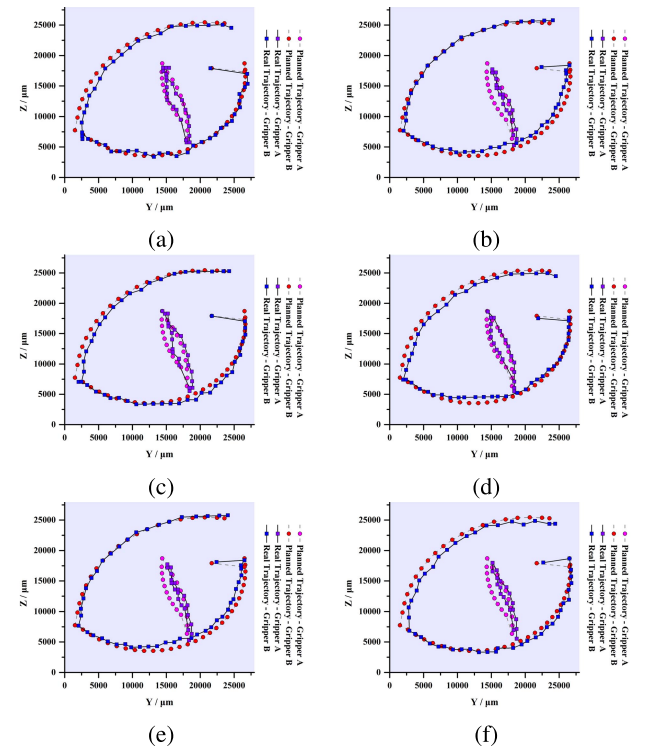


Fig. 20. Planned and real trajectories in the experiment. (a)–(f) Trajectories from Group 1 to Group 6.

visual feedback, inputs to the manipulators were computed using the LQ control method. Snapshots from one trial of the suture looping were shown in Fig. 19.

It can be noticed that two grippers followed their designed paths, and one loop was successfully constructed around Gripper A, consuming an average time around 408 s. In addition, suture slippage or collision did not occur during the operation. To comprehensively demonstrate the proposed approach, six trials of suture looping manipulation were conducted. The planned trajectories, as well as the trajectories of the grippers evaluated from the vision information, were shown in Fig. 20. Calculating the mean values of the time-dependent errors in these trials, outcomes were listed in Table IV. Besides, errors via time steps were shown in Fig. 21.

When adding the surgical suture to the process, larger deviations between the two trajectories can be observed.

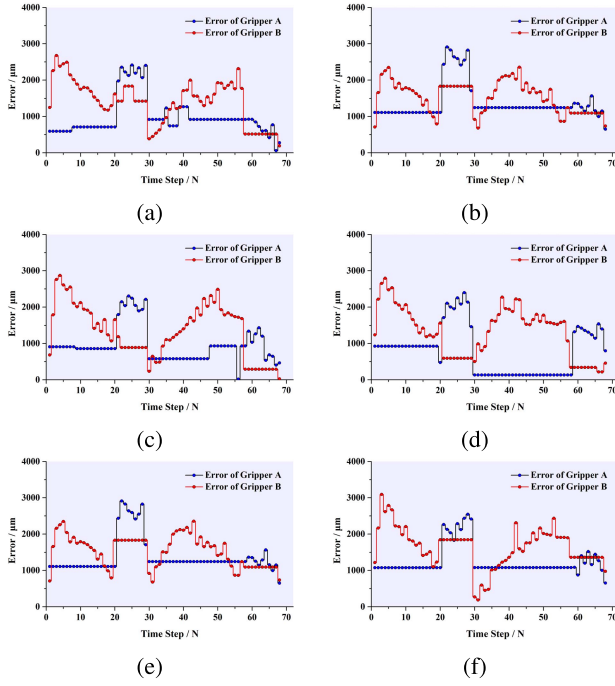


Fig. 21. Experimental errors between the planned and real trajectories via time steps. (a)–(f) Experimental data from Group 1 to Group 6.

TABLE IV

MEAN VALUES OF STEP ERRORS IN THE SUTURE LOOPING PROCEDURES;
PARAMETERS: $T_1 = 5$, $T_2 = 0.1$; UNIT: MICROMETERS

Experiment	1	2	3	4	5	6
Gripper A	987	1369	955	779	1369	1243
Gripper B	1402	1538	1340	1312	1538	1640

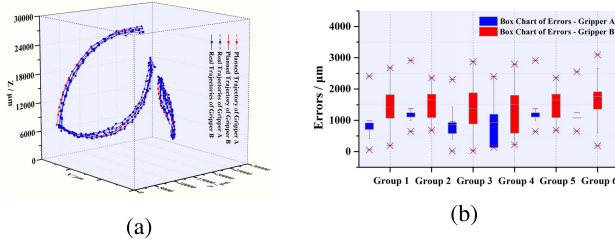


Fig. 22. (a) Planned trajectory and six groups of real trajectories obtained in the experiment. (b) Error distributions of gripper A and B in six suture looping manipulations.

The increase in the tracking error was mainly due to the tension force to shift the gripper position. Slight variations in the preload tension in the suture between the six trials also caused discrepancies in the position errors as shown in Figs. 20 and 21. Treating X -coordinates of two grippers as fixed values, the spatial trajectories of grippers in six trials were sketched in Fig. 22(a). With all error data, error distributions of two grippers were illustrated in Fig. 22(b).

In Table IV, the average step errors of Gripper A and B in six experiments were 1.1 and 1.5 mm, respectively. Gripper B had larger errors, which was due to its longer travel distance in the operation. Despite these errors, two grippers still successfully

followed the planned paths and completed six trials, and no suture slippage or collision occurred.

V. CONCLUSION

In this paper, a complete set of solutions was proposed toward automating the suture looping procedure in surgical knot tying. Performances of the looping process through an in-house robotic system were carefully excogitated and investigated. To design efficient and reliable trajectories that were feasible to the task of suture looping, especially to the wound suturing scenario, equations leading the grippers to complete the procedure were formulated. The grippers of the system were coordinated such that the workspace required to construct the suture loop could be reduced, while issues such as suture slippage and collision could be eliminated. By mapping the coordinates between the image and the robot frames, the real-time positions of the grippers were evaluated from the camera and fed to the LQ control scheme to generate the inputs to the system. In the experiments, the accuracy of the object detection algorithm was validated, and different groups of tuning parameters for the LQ controller were investigated. The robustness of the control approach was examined by testing the performance of the system under external impulse disturbances and the lost track conditions during the looping process. The robotic system was examined to carry out the entire task, and the suture looping operations can be successfully conducted in all six trials, which validate the feasibility of the entire vision-based control system. This paper provides a simple and efficient method to automate the tedious suture loop process and also proves a promising future of standardizing and automating similar subtasks in surgery using robots

REFERENCES

- [1] R. H. Taylor, A. Menciassi, G. Fichtinger, P. Fiorini, and P. Dario, "Medical robotics and computer-integrated surgery," in *Springer Handbook of Robotics*. Cham, Switzerland: Springer, 2016.
- [2] G. H. Ballantyne, "Robotic surgery, telerobotic surgery, telepresence, and telementoring," *Surgical Endoscopy Interventional Techn.*, vol. 16, no. 10, pp. 1389–1402, 2002.
- [3] A. R. Lanfranco, A. E. Castellanos, J. P. Desai, and W. C. Meyers, "Robotic surgery: A current perspective," *Ann. Surg.*, vol. 239, no. 1, pp. 14–21, Jan. 2004.
- [4] H. Mayer, I. Nagy, A. Knoll, E. U. Schirmbeck, and R. Bauernschmitt, "An experimental system for robotic heart surgery," in *Proc. IEEE 18th Int. Symp. Comput.-Based Med. Syst.*, 2005, pp. 55–60.
- [5] P. Hynes, G. I. Dodds, and A. J. Wilkinson, "Uncalibrated visual-servoing of a dual-arm robot for MIS suturing," in *Proc. 1st IEEE/RAS-EMBS Int. Conf. Biomed. Robot. Biomechatronics*, 2006, pp. 420–425.
- [6] W. R. Chitwood, Jr., et al., "Robotic mitral valve repair: Trapezoidal resection and prosthetic annuloplasty with the da Vinci surgical system," *J. Thoracic Cardiovascular Surg.*, vol. 120, no. 6, pp. 1171–1172, 2000.
- [7] G. T. Sung and I. S. Gill, "Robotic laparoscopic surgery: A comparison of the da Vinci and Zeus systems," *Urology*, vol. 58, no. 6, pp. 893–898, 2001.
- [8] C. C. Abbou et al., "Laparoscopic radical prostatectomy with a remote controlled robot," *J. Urol.*, vol. 165, pp. 1964–1966, Jun. 2001.
- [9] A. Tewari, J. O. Peabody, R. Sarle, A. K. Hemal, A. Shrivastava, and M. Menon, "Technique of da Vinci robot-assisted anatomic radical prostatectomy," *Urology*, vol. 60, no. 4, pp. 569–572, 2002.
- [10] J. Bodner, H. Wykypiel, G. Wetscher, and T. Schmid, "First experiences with the da Vinci operating robot in thoracic surgery," *Eur. J. Cardio-Thoracic Surg.*, vol. 25, no. 5, pp. 844–851, 2004.
- [11] E. J. Hanly and M. A. Talamini, "Robotic abdominal surgery," *Amer. J. Surg.*, vol. 188, no. 4, pp. 19–26, Oct. 2004.
- [12] S. W. Kang et al., "Robotic thyroid surgery using a gasless, transaxillary approach and the da Vinci S system: The operative outcomes of 338 consecutive patients," *Surgery*, vol. 146, pp. 1048–1055, Dec. 2009.

- [13] P. C. Julianotti *et al.*, "Robotics in general surgery: Personal experience in a large community hospital," *Arch. Surg.*, vol. 138, no. 7, pp. 777–784, 2003.
- [14] J. R. R. Mayer and G. A. Parker, "A portable instrument for 3-D dynamic robot measurements using triangulation and laser tracking," *IEEE Trans. Robot. Autom.*, vol. 10, no. 4, pp. 504–516, Aug. 1994.
- [15] M. T. El-Haddad and Y. K. Tao, "Automated stereo vision instrument tracking for intraoperative OCT guided anterior segment ophthalmic surgical maneuvers," *Biomed. Opt. Express*, vol. 6, no. 8, pp. 3014–3031, 2015.
- [16] H. K. Chu, J. K. Mills, and W. L. Cleghorn, "Image-based visual servoing through micropart reflection for the microassembly process," *J. Micromech. Microeng.*, vol. 21, no. 6, p. 065016, 2011.
- [17] B. Espiau, F. Chaumette, and P. Rives, "A new approach to visual servoing in robotics," *IEEE Trans. Robot. Autom.*, vol. 8, no. 3, pp. 313–328, Jun. 1992.
- [18] D. Putzer, S. Klug, J. L. Moctezuma, and M. Nogler, "The use of time-of-flight camera for navigating robots in computer-aided surgery: Monitoring the soft tissue envelope of minimally invasive hip approach in a cadaver study," *Surg. Innov.*, vol. 21, no. 6, pp. 630–636, 2014.
- [19] B. Puciński, J. Juszczak, P. Bożek, J. Ciekański, J. Dzielicki, and E. Pietka, "Image navigation in minimally invasive surgery," in *Information Technologies in Biomedicine (Advances in Intelligent Systems and Computing)*, vol. 248. 2014, pp. 25–34, doi: [10.1007/978-3-319-06596-0_3](https://doi.org/10.1007/978-3-319-06596-0_3)
- [20] J. D. James, M. M. Wu, E. K. Batra, G. T. Rodeheaver, and R. F. Edlich, "Technical considerations in manual and instrument tying techniques," *J. Emergency Med.*, vol. 10, no. 4, pp. 469–480, 1992.
- [21] B. Ekçi, "A simple technique for knot tying in single incision laparoscopic surgery (SILS)," *Clinics*, vol. 65, no. 10, pp. 1055–1057, 2010.
- [22] D.-L. Chow and W. Newman, "Improved knot-tying methods for autonomous robot surgery," in *Proc. IEEE Int. Conf. Automat. Sci. Eng.*, Aug. 2013, pp. 461–465.
- [23] H. Mayer, F. Gomez, D. Wierstra, I. Nagy, A. Knoll, and J. Schmidhuber, "A system for robotic heart surgery that learns to tie knots using recurrent neural networks," *Adv. Robot.*, vol. 22, nos. 13–14, pp. 1521–1537, 2008.
- [24] E. Croce and S. Olmi, "Intracorporeal knot-tying and suturing techniques in laparoscopic surgery: Technical details," *J. Soc. Laparoendoscopic Surgeons*, vol. 4, no. 1, pp. 17–22, 2000.
- [25] R. R. Gopaldas and R. M. Reul, "Intracorporeal knot-tying for the thoracoscopic surgeon: A novel and simplified technique," *Texas Heart Inst. J.*, vol. 37, no. 4, pp. 435–438, 2010.
- [26] K. A. Guru, M. R. Sheikh, S. J. Raza, A. P. Stegemann, and J. Nyquist, "Novel knot tying technique for robot-assisted surgery," *Can. J. Urol.*, vol. 19, no. 4, pp. 6401–6403, 2012.
- [27] T. Muffly, T. C. McCormick, J. Dean, A. Bonham, and R. F. Hill, "An evaluation of knot integrity when tied robotically and conventionally," *Amer. J. Obstetrics*, vol. 200, no. 5, pp. e18–e20, 2009.
- [28] S. Wang, H. Wang, and L. Yue, "A novel knot-tying approach for minimally invasive surgical robot systems," *Int. J. Med. Robot. Comput. Assist. Surg.*, vol. 4, no. 3, pp. 268–276, 2008.
- [29] D. L. Murphy, "Endoscopic suturing and knot tying: Theory into practice," *Ann. Surg.*, vol. 234, no. 5, pp. 607–612, 2001.
- [30] M. P. Bell, W. Wang, J. Kunzika, and D. Balkcom, "Knot-tying with four-piece fixtures," *Int. J. Robot. Res.*, vol. 33, no. 11, pp. 1481–1489, 2014.
- [31] H. Kang and J. T. Wen, "Robotic assistants aid surgeons during minimally invasive procedures," *IEEE Eng. Med. Biol. Mag.*, vol. 20, no. 1, pp. 94–104, Jan./Feb. 2001.
- [32] N. Padov and G. D. Hager, "Human-Machine Collaborative surgery using learned models," in *Proc. IEEE Conf. Robot. Autom.*, May 2011, pp. 5285–5292.
- [33] J. van den Berg *et al.*, "Superhuman performance of surgical tasks by robots using iterative learning from human-guided demonstrations," in *Proc. Int. Conf. Robot. Automat.*, 2010, pp. 2074–2081.
- [34] T. Osa, K. Harada, N. Sugita, and M. Mitsuishi, "Trajectory planning under different initial conditions for surgical task automation by learning from demonstration," in *Proc. IEEE Int. Conf. Robot. Autom.*, May/Jun. 2014, pp. 6507–6513.
- [35] H. Mayer *et al.*, "Automation of manual tasks for minimally invasive surgery," in *Proc. 4th Int. Conf. Autonomic Auton. Syst.*, 2008, pp. 260–265.
- [36] J. Takamatsu, T. Morita, K. Ogawara, H. Kimura, and K. Ikeuchi, "Representation for knot-tying tasks," *IEEE Trans. Robot.*, vol. 22, no. 1, pp. 65–78, Feb. 2006.
- [37] S. Sen, A. Garg, D. V. Gealy, S. McKinley, Y. Jen, and K. Goldberg, "Automating multi-throw multilateral surgical suturing with a mechanical needle guide and sequential convex optimization," in *Proc. Int. Conf. Robot. Automat.*, 2016, pp. 4178–4185.
- [38] F. Nageotte, P. Zanne, M. de Mathelin, and C. Doignon, "A circular needle path planning method for suturing in laparoscopic surgery," in *Proc. IEEE Int. Conf. Robot. Automat.*, Apr. 2005, pp. 514–519.
- [39] S. P. DiMaio and S. E. Salcudean, "Needle steering and model-based trajectory planning," in *Proc. Int. Conf. Med. Image Comput. Comput.-Assist. Intervent.*, 2003, pp. 33–40.
- [40] B. D. Argall, S. Chernova, M. Veloso, and B. Browning, "A survey of robot learning from demonstration," *Robot. Auto. Syst.*, vol. 57, no. 5, pp. 469–483, 2009.
- [41] A. Gasparetto, P. Boscaroli, A. Lanzutti, and R. Vidoni, "Trajectory planning in robotics," *Math. Comput. Sci.*, vol. 6, no. 3, pp. 269–279, 2012.
- [42] B. Lu, H. K. Chu, and L. Cheng, "Dynamic trajectory planning for robotic knot tying," in *Proc. IEEE Int. Conf. Real-Time Comput. Robot.*, Jun. 2016, pp. 180–185.
- [43] H. Kang and J. T. Wen, "Autonomous suturing using minimally invasive surgical robots," in *Proc. IEEE Int. Conf. Control Appl.*, Sep. 2000, pp. 742–747.
- [44] D.-L. Chow and W. Newman, "Trajectory optimization of robotic suturing," in *Proc. IEEE Int. Conf. Technol. Practical Robot Appl.*, May 2015, pp. 1–6.
- [45] B. Lu, H. K. Chu, and L. Cheng, "Robotic knot tying through a spatial trajectory with a visual servoing system," in *Proc. IEEE/RSJ Int. Conf. Intell. Robots Syst.*, Sep. 2017, pp. 5710–5716.
- [46] A. M. McIvor, "Background subtraction techniques," in *Proc. Image Vis. Comput.*, 2000, pp. 3099–3104.
- [47] M. Piccardi, "Background subtraction techniques: A review," in *Proc. IEEE Int. Conf. Syst., Man Cybern.*, Oct. 2004, pp. 3099–3104.
- [48] J. P. Lewis, "Fast template matching," *Vis. Interface*, vol. 95, pp. 15–19, May 1995.
- [49] H. Kang and J. T. Wen, "Robotic knot tying in minimally invasive surgeries," in *Proc. Int. Conf. Intell. Robots Syst.*, vol. 2, 2002, pp. 1421–1426.
- [50] J. T. Feddema, C. S. G. Lee, and O. R. Mitchell, "Automatic selection of image features for visual servoing of a robot manipulator," in *Proc. IEEE Int. Conf. Robot. Automat.*, May 1989, pp. 832–837.
- [51] T. R. Oliveira, A. C. Leite, A. J. Peixoto, and L. Hsu, "Overcoming limitations of uncalibrated robotics visual servoing by means of sliding mode control and switching monitoring scheme," *Asian J. Control*, vol. 16, no. 3, pp. 752–764, May 2014.
- [52] B. E. Bishop and M. W. Spong, "Adaptive calibration and control of 2D monocular visual servo systems," *IFAC Robot Control*, vol. 30, no. 20, pp. 505–510, 1997.
- [53] Y. Wu, S. Jiang, Z. Xu, S. Zhu, and D. Cao, "Lens distortion correction based on one chessboard pattern image," *Frontiers Optoelectron.*, vol. 8, no. 3, pp. 319–328, 2015.
- [54] L. Wang, L. Ren, J. K. Mills, and W. L. Cleghorn, "Automated 3-D micrograsping tasks performed by vision-based control," *IEEE Trans. Autom. Sci. Eng.*, vol. 7, no. 3, pp. 417–426, Jul. 2010.
- [55] Y. Sun and B. J. Nelson, "Biological cell injection using an autonomous microrobotic system," *Int. J. Robot. Res.*, vol. 21, nos. 10–11, pp. 861–868, 2002.
- [56] H. Bilen, M. Hocaoglu, E. Ozgur, M. Unel, and A. Sabanovic, "A comparative study of conventional visual servoing schemes in microsystem applications," in *Proc. IEEE/RSJ Int. Conf. Intell. Robots Syst.*, Oct./Nov. 2007, pp. 1308–1313.
- [57] B. Nelson, N. P. Papanikopoulos, and P. K. Khosla, "Visual servoing for robotic assembly," in *Visual Servoing: Real-Time Control of Robot Manipulators Based on Visual Sensory Feedback*. River Edge, NJ, USA: World Scientific, 1993, pp. 139–164.



Bo Lu received the B.Eng. degree from the Dalian University of Technology, Dalian Shi, Liaoning Sheng, China, in 2013, and the M.S. degree (Hons.) from The Hong Kong Polytechnic University, Hong Kong, in 2015, where he is currently pursuing the Ph.D. degree with the Department of Mechanical Engineering.

His research interests include surgical robots, automation and control, trajectory plan, computer vision, and surgical tool detection.



Henry K. Chu (M'12) received the B.S. degree in mechanical engineering from the University of Waterloo, Waterloo, ON, Canada, in 2005, and the M.S. and Ph.D. degrees in mechanical and industrial engineering from the University of Toronto, Toronto, ON, Canada, in 2007 and 2011, respectively.

He was a Post-Doctoral Fellow with the University of Toronto and the City University of Hong Kong, Hong Kong. He is currently an Assistant Professor with The Hong Kong Polytechnic University, Hong Kong. His research interests include robotic manipulation, vision-based control and automation, microsystem design, and tissue engineering.



Li Cheng received the B.S. degree from Xi'an Jiaotong University, Xi'an, China, and the DEA and Ph.D. degrees from the Institute National des Sciences Appliques de Lyon, Lyon, France.

He is currently the Chair Professor of Mechanical Engineering and the Director of Consortium for Sound and Vibration Research with The Hong Kong Polytechnic University, Hong Kong. He was with Laval University, Quebec City, QC, Canada, in 1992, where he became an Assistant Professor and Associate/Full Professor, the Chair Professor in 2005, and the Head of the Department from 2011 to 2014. He works in the field of sound and vibration, structural health monitoring, and smart structure and control.

Dr. Cheng is an Elected Fellow of the Acoustical Society of America, Acoustical Society of China, IMechE, Hong Kong Institution of Engineers, and the Hong Kong Institute of Acoustics. He currently serves as the Deputy Editor-in-Chief and a Receiving Editor for the *Journal of Sound and Vibration* and an Associate Editor for the *Journal of Acoustical Society of America*.



K. C. Huang received the B.Eng. degree from the Department of Automation, Shenzhen University, Shenzhen, Guangdong, China, in 2014, and the M.Sc. degree in mechanical and automation engineering, Chinese University of Hong Kong, Hong Kong, in 2015. He is currently pursuing the Ph.D. degree with The Hong Kong Polytechnic University, Hong Kong.

His research interests include cell patterning with dielectrophoresis.